



Bifunctional porous SnO₂/Ag nanofibers for efficient electroreduction of carbon dioxide to formate and its mechanism elucidation by in-situ surface-enhanced Raman scattering

Junjie Chen^a, Benhua Ma^a, Zhoubing Xie^b, Weimo Li^c, Yumei Yang^a, Ming Mu^a, Xiaoxin Zou^b, Bing Zhao^a, Wei Song^{a,*}

^a State Key Laboratory of Supramolecular Structure and Materials, College of Chemistry, Jilin University, Changchun 130012, PR China

^b State Key Laboratory of Inorganic Synthesis and Preparative Chemistry, College of Chemistry, Jilin University, Changchun 130012, PR China

^c Alan G. MacDiarmid Institute, College of Chemistry, Jilin University, 2699 Qianjin Street, Changchun 130012, PR China

ARTICLE INFO

Keywords:

CO₂ electroreduction
In-situ SERS spectroscopy
Bifunctional nanofibers
Mechanism elucidation
Sn-based catalysts

ABSTRACT

Monitoring the reaction intermediates and revealing the real active sites are of great importance for elucidation mechanism and designing ideal catalysts. Here, bifunctional porous SnO₂/Ag nanofibers (P-SnO₂/Ag) are prepared and present high Faradaic efficiency (FE) of 92.4% for formate with a current density of 24.6 mA cm⁻² at -0.9 V (vs. RHE). The in-situ SERS spectra reveal that tin-oxide in P-SnO₂/Ag nanofibers are easy reduced, indicates metallic tin likely be the real active site rather than Sn (IV) and Sn (II) oxide species in CO₂RR. The characteristic SERS peak at around 1420 cm⁻¹ corresponding to the key *OCHO* intermediate for HCOO⁻ production is also captured, favorably formed after the first *CO₂* intermediate suitably adsorbed on P-SnO₂/Ag nanofibers via oxygen atoms. Combining the intrinsic SERS properties and excellent catalytic performance of P-SnO₂/Ag nanofibers, a real correlation is established between the composition and chemical structure of the materials and their catalytic performance.

1. Introduction

To ensure the rapid development of industry, the use of fossil fuels has caused a sharp rise in the level of CO₂, a typical greenhouse gas in the atmosphere, leading to the problems such as global warming, climate change, and ocean acidification [1,2]. Electrocatalytic technology has been widely developed to reduce CO₂ into value-added chemicals or fuels due to the advantages of mild reaction conditions, operational simplicity, and the potential for coupling with clean and renewable energy technologies [3,4]. Among the products of electrocatalytic CO₂ reduction reaction (CO₂RR), formic (HCOO⁻) production via a two-electron transfer pathway is highly desirable owing to its convenience of storage, feasibility of long-range transport and broad application in industrial feedstock [5,6]. Recently, a variety of heterogeneous electrocatalysts based on Sn, Pd, Pb, Bi and In have shown relatively high selectivity for converting CO₂ to HCOO⁻ [7,8]. Among them, Sn and Sn-based oxide nanostructures have captured extensive attention due to their suitable binding strength with specific intermediates, low toxicity and cheapness [9–12]. Whereas, they still

suffer from intrinsically poor catalytic activity and low electrical conductivity, and there are debate about the electrocatalytic mechanism and actual active sites of Sn-based catalysts [10,13,14]. The integration of metals and metal oxides is an attractive strategy for optimizing the binding strength of key intermediates and thereby enhance the electrocatalytic activity [14,15]. An ideal catalyst needs to directional maximize the selectivity of formic over other CO₂RR products and hydrogen at the reduction potential. Furthermore, in-situ or operated unveiling the actual catalytically active sites and monitoring the reaction intermediates are of great importance for understanding the reaction mechanism, which is beneficial to design catalysts with large catalytic activity, high selectivity and desirable stability [16,17].

Surface-enhanced Raman scattering (SERS) exhibits a high sensitivity, remarkable selectivity, short signal acquisition time, and simplicity for operation, which provides a highly specific fingerprint-like spectrum [18,19]. These characteristics endowed SERS to play an increasingly important role in scientific research, especially in understanding various catalytic processes and reaction mechanism [20,21]. As early as 1995, Ichinohe et al. successfully used SERS to study CO₂RR

* Corresponding author.

E-mail address: weisong@jlu.edu.cn (W. Song).

<https://doi.org/10.1016/j.apcatb.2022.122350>

Received 12 October 2022; Received in revised form 30 November 2022; Accepted 29 December 2022

Available online 31 December 2022

0926-3373/© 2023 Elsevier B.V. All rights reserved.

process at noble metal electrodes [22], and in 2018, Chernyshova [16] et al. demonstrated that the SERS spectroscopy can monitor the reaction intermediates in the CO₂RR process at rough copper electrode. Very recently, shell-isolated nanoparticle-enhanced Raman spectroscopy (SHINERS) was used to elucidate the CO₂RR mechanisms on atomically flat single-crystal surfaces [23]. SERS spectroscopy has been shown to be very powerful in studying CO₂RR process at specific electrode surfaces, but it is still challenging to study actual catalysts with high catalytic activity with SERS, because such catalysts are often complex and multi-component.

Apart from tailoring the compositions of catalysts, the fabrication of catalysts with a porous structure is another promising strategy to enhance the catalytic activity via the exposing more active sites [24–27]. Herein, we demonstrated the facile fabrication of porous SnO₂/Ag composite nanofibers (P-SnO₂/Ag nanofibers) via an electrospinning and subsequent two-step calcination process to exhibit excellent electrocatalytic performance for CO₂RR and SERS property. On the one hand, the porous structure and the synergistic effect from the interaction between SnO₂ and Ag endow the P-SnO₂/Ag nanofibers with a highest Faradaic efficiency (FE) of 92.4% for HCOO[−] and a current density of 24.6 mA cm^{−2} at −0.9 V (vs. reversible hydrogen electrode (RHE)), possessed a high FE of C1 products (>80%) from −0.8 to −1.2 V (vs. RHE). In addition, P-SnO₂/Ag nanofibers can stably operate more than 10 h at −0.9 V (vs. RHE) with negligible loss in current density and FE. One the other hand, the in-situ SERS spectra not only revealed that the P-SnO₂/Ag nanofibers were more easily reduced than porous SnO₂ fibers but also provided direct spectroscopic evidence that the adsorption strength and adsorption mode of the *CO₂ intermediate directly affected the subsequent reaction intermediates and the selectivity of the catalytic reaction. Firstly, the *CO₂ intermediate is first generated in both CO and HCOO[−] generation from CO₂ and is the rate-limiting step for CO₂RR. Secondly, when P-SnO₂/Ag nanofibers are used as a catalyst, the characteristic SERS peak at around 1420 cm^{−1} attributed to the *OCHO intermediate is captured, which is adsorbed on the catalyst via the oxygen atoms and favors the formation of HCOO[−]. By contrast, *CO₂ intermediate is tightly adsorbed to P-Ag nanofibers through carbon atoms, which favors the formation of CO via *COOH intermediates.

2. Experimental details

2.1. Chemicals and materials

Tin (II) chloride dihydrate (SnCl₂·2 H₂O, 99%) and silver nitrate (AgNO₃, 99%) were purchased from Sinopharm Chemical Reagent Co. Ltd. Polyacrylonitrile (PAN, Mw = 80,000) and polystyrene (PS, Mw = 56,000) were bought from the Jilin Chemical Plant. *p*-Aminothiophenol (PATP), 4-Mercaptopyridine (MPY) and Leucocrystal violet (CV) were available from Sigma-Aldrich. N,N-Dimethylformamide (DMF), potassium hydroxide (KOH), Ethanol and potassium bicarbonate (KHCO₃) were purchased from Beijing Chemical Works. All the chemicals mentioned above were used as received without further purification.

2.2. Preparation of the P-SnO₂/Ag nanofibers

In a representative experiment is illustrated in Scheme S1, 0.25 g of PAN and 0.25 g of PS were first dissolved in 4.5 g of DMF under stirring for 12 h at room temperature to obtain a clear homogeneous solution. Afterward, 0.25 g of SnCl₂·2 H₂O and 0.25 g of AgNO₃ were added and stirred vigorously for another 12 h. The obtained electrospinning precursor was used directly for electrospinning with the distance of 20 cm between the spinneret (the anode) and the aluminum foil-covered drum collector (the cathode) under a high voltage of 18 kV. Then the nanofibrous precursor membrane was obtained and allowed to dry at 30 °C for 12 h. To prepare P-SnO₂/Ag nanofibers, the nanofibrous precursor membrane was calcined at a temperature of 300 °C in a horizontal quartz tube furnace for 2 h with a heating rate of 2 °C min^{−1} from room

temperature in air and then annealed at 800 °C for 2 h with a heating rate of 5 °C min^{−1}. For other control samples, the ones with only 0.5 g of SnCl₂·2 H₂O or only 0.5 g of AgNO₃ as inorganic salts were named as P-Ag and P-SnO₂, respectively, and the sample without PS compared to P-SnO₂/Ag is named SnO₂/Ag.

2.3. Characterization

Field-emission scanning emission microscopy (FESEM, FEI Nova NanoSEM) and Transmission microscope (TEM, JEM-2100 F) at 200 kV were used to explore the morphologies of the as-synthesized samples. The crystal structures and chemical composition were confirmed by X-ray diffraction (XRD, PANalytical B.V. Empyrean) with Cu Kα radiation and X-ray photoelectron spectrometer (XPS, Thermo ESCALAB 250), respectively. The contents of Ag and Sn were characterized by Inductively coupled plasma spectrometry (ICP, Agilent 725). The resistivity measurements of the prepared nanofibers were performed with van der Pauw configuration at room temperature (Lake Shore 7704 A Hall measurement system). The liquid products and gas product were quantified by 500 MHz ¹H NMR (Bruker 500) and on-line GC (Agilent 7890B), respectively.

2.4. Electrochemical measurements

All the electrochemical measurements were carried out in a H-type cell with two compartments separated by a piece of cation exchange membrane (Nafion 117, Dupont). Each compartment is held in 40 mL of 0.5 M KHCO₃ electrolyte and pre-saturated with N₂ or CO₂ for at least 30 min before all electrochemical experiments at a rate of 50 mL min^{−1}. And during the electrochemical experiments, the flow rate of the gas is stably controlled at 30 mL min^{−1} by using a gas mass flow meter (AST10, ASERT). The carbon paper (HCP020P, Shanghai Hesen Electrical Co., Ltd.) loaded with different catalysts was used as working electrode and a platinum foil and an Ag/AgCl electrode (saturated NaCl) were served as the counter electrode and the reference electrode, respectively. To prepare the working electrode, 4.0 mg of the obtained catalyst and 20 μL of 5 wt% Nafion solution were dispersed in 680 μL of DI water and 300 μL of ethanol under a bath-sonication for 2 h to form a homogenous catalyst ink. Then 50 μL of the ink was dropped onto a 0.4 × 0.5 cm² carbon paper and dried at room temperature to obtain the working electrode with a mass loading of 1 mg cm^{−2}. All potentials are reported with respect to the reversible hydrogen electrode (RHE) according to Eq.1.

$$E(\text{vs. RHE}) = E(\text{vs. Ag/AgCl}) + 0.198V + 0.059 \times \text{pH} \quad (1)$$

where E (vs. RHE), E (vs. Ag/AgCl), and pH are the potential vs. RHE, the measured potential vs. the Ag/AgCl reference electrode, and pH of the electrolyte.

2.5. Product analysis

To determine the reduction products and the selectivity of the catalyst, the liquid products and gas product were quantified by 500 MHz ¹H NMR (Bruker 500) and on-line GC (Agilent 7890B), respectively. Faradaic efficiency (FE) is described as the percentage of electrons consumed to produce the target product, which can be understood as the selectivity of the catalyst of this product.

The FE of each gas product were calculated according to the Eq.2.

$$FE(\%) = \frac{Q_{\text{product}}}{Q_{\text{total}}} = \frac{N \times F \times v_0 \times P_0 \times \nu}{j \times R \times T} \times 100\% \quad (2)$$

Where N is the number of electrons transferred from CO₂ to a molecule of target product. F is the Faraday constant (96,485 C mol^{−1}). *v*₀ is the volume concentration of the gas products (ppm). *P*₀ is the standard atmospheric pressure (101.325 kPa). *ν* is the gas flow rate

(30 sc.c.m.). R is the universal gas constant ($8.314 \text{ J mol}^{-1} \text{ K}^{-1}$). T is the system temperature (298.15 K). And j is the steady-state current.

The FE of each liquid products were calculated according to the Eq.3.

$$FE(\%) = \frac{Q_{\text{product}}}{Q_{\text{total}}} = \frac{N \times F \times c \times V}{Q_{\text{total}}} \times 100\% \quad (3)$$

Where N is the number of electrons transferred from CO_2 to a molecule of target product. F is the Faraday constant ($96,485 \text{ C mol}^{-1}$). c is the concentration of target product in the electrolyte (mol L^{-1}). V is the volume of the electrolyte (mL). Q_{total} is the accumulated charge during the galvanostatic measurement.

2.6. In-situ SERS measurements

In order to collect in-situ SERS spectra in the electrocatalysis process, we built up an inverted Raman spectroscopy system, which combines a PI spectrometer (PIX2560-SF-Q), 532 nm laser (MSL-III-532 nm-100Mw-19021075) and Olympus inverted microscope (IX73). The in-situ SERS spectra were recorded after each constant potential was applied for 150 s. The intensity of the laser is controlled at 2 mW with attenuation by a filter to avoid laser-induced modifications of the catalyst. Each Raman spectrum was acquired with 10 s exposure time per scan with three consecutive scans with single window acquisition mode under different applied potentials spanning from open circuit

potential (OCP) to -1.2 V vs. RHE. In order to verify the reliability of the data, we have used nanofibers prepared in different batches as catalysts to be performed in-situ electrochemical SERS experiments. And we calibrated the energy shift using a Si wafer to ensure high confidence and reproducibility of the SERS spectra.

3. Results and discussion

3.1. Morphological and structural characterizations

The typical synthetic procedure of the $\text{P-SnO}_2/\text{Ag}$ nanofibers is illustrated in Scheme S1. Firstly, a precursor membrane has been prepared by electrospinning a mixing dispersion consisting of PAN, PS, $\text{SnCl}_2 \cdot 2\text{H}_2\text{O}$ and AgNO_3 in N,N -Dimethylformamide (DMF) solvent. The morphology of the electrospun precursor membrane is revealed by field-emission scanning electron microscopy (FESEM). As shown in Fig. S1, the obtained pristine precursor membrane exhibits a smooth fiber-like morphology, with average diameters of around 260 nm. Subsequently, $\text{P-SnO}_2/\text{Ag}$ nanofibers can be prepared via an annealing and calcination treatment of the as-prepared precursor membrane at a temperature of 300°C and 800°C in air to remove PS and PAN, respectively. Typically, the resultant $\text{P-SnO}_2/\text{Ag}$ product still maintains a fibrous morphology with interconnected porous structure and exhibits a diameter ranging from 150 to 200 nm (Fig. 1a). By contrast, solid

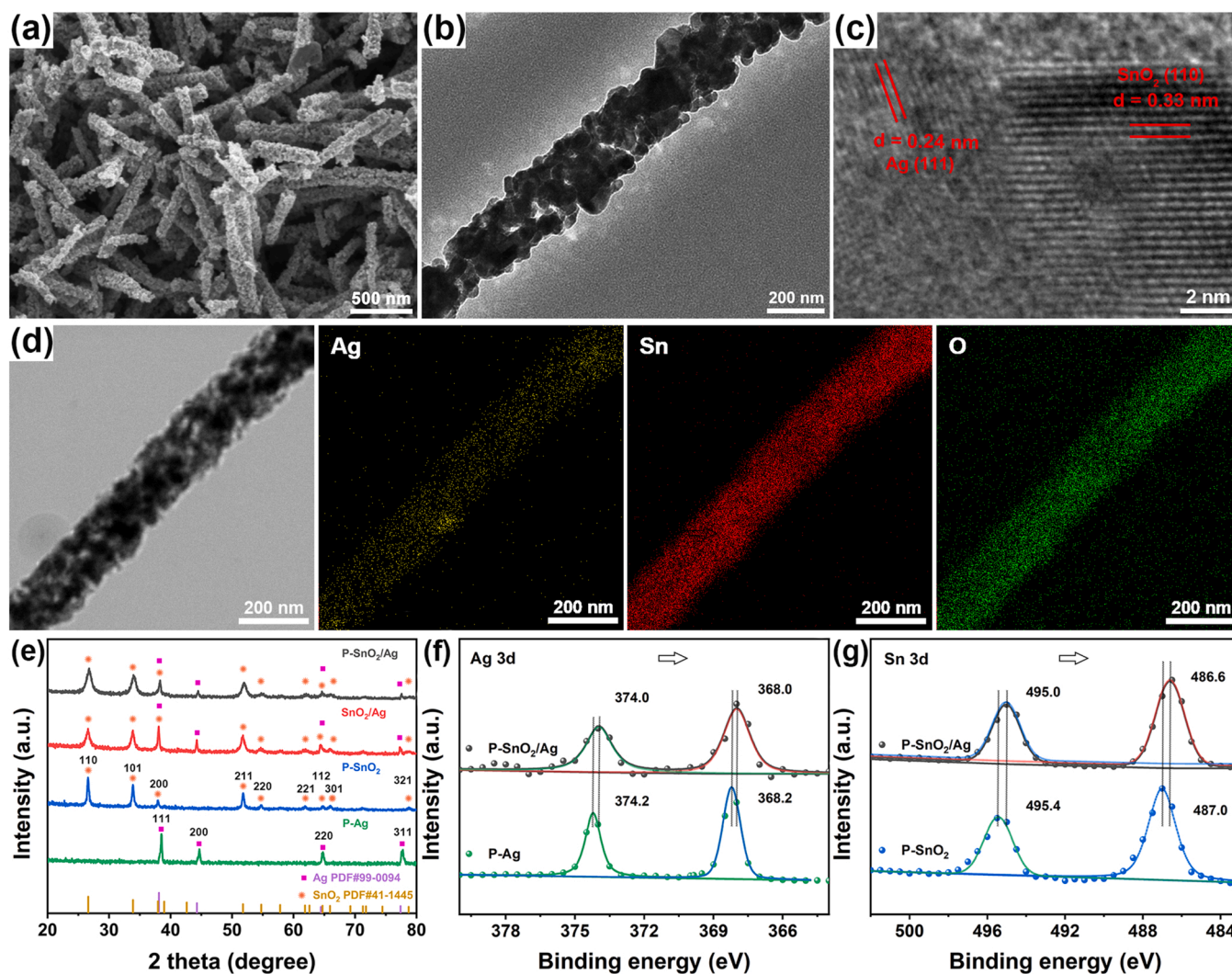


Fig. 1. (a) SEM, (b) TEM and (c) HRTEM images of $\text{P-SnO}_2/\text{Ag}$ nanofibers. (d) HAADF and EDX-mappings of $\text{P-SnO}_2/\text{Ag}$ nanofibers. (e) XRD patterns of the $\text{P-SnO}_2/\text{Ag}$ (black), SnO_2/Ag (red), P-SnO_2 (blue) and P-Ag (green) nanofibers. (f) Typical Ag 3d and (g) Sn 3d XPS spectra for P-Ag , P-SnO_2 and $\text{P-SnO}_2/\text{Ag}$ nanofibers.

SnO₂/Ag nanofiber has also been prepared in the absence of PS in the precursor. As shown in Fig. S2a, the SEM image shows that the SnO₂/Ag composite densely assembles together to form nanofibers with diameters of 250–300 nm. In the case of P-SnO₂ nanofibers, it maintains a similar morphology to P-SnO₂/Ag nanofibers, while the diameter of the fibers (200–300 nm) is a little larger than that of P-SnO₂/Ag nanofibers (Fig. S2b). On the other hand, as shown in Fig. S2c, in the absence of SnCl₂·2 H₂O, metallic Ag partially melts at 800 °C and further form coral-like P-Ag. The formation mechanism of the interconnected porous structure of P-SnO₂/Ag nanofibers can be explained from the following two aspects. On the one hand, the sacrificial PS templates are decomposed at around 300 °C, resulting in the formation of macro pores [28], which is beneficial to expose the electrochemical active sites. On the other hand, Tin ions are heated in the air to form SnO₂ nanoparticles via the crystallization and diffusion, which is further assembled into nanofibers templated by the electrospun precursor nanofibers [29]. In the case of P-SnO₂/Ag nanofibers, the Ag source is reduced to metallic Ag during the higher temperature calcination step (800 °C), which effectively improve the electrical conductivity [30]. Inductively coupled plasma (ICP) result shows that the molar ratio of Ag to Sn in P-SnO₂/Ag nanofibers after calcination at 800 °C is 2.47, which is a little different with that of the feed molar ratio of Ag/Sn because of the AgCl enrichment is formed in the precursors before the electrospinning process (Fig. S11). The resistivity measurements of the prepared nanofibers are performed with van der Pauw configuration by Lake Shore 7704 A Hall measurement system at room temperature. As shown in Fig. S3, the P-SnO₂/Ag nanofibers exhibits a much lower resistivity than that of P-SnO₂ nanofibers and similar with those of SnO₂/Ag and P-Ag samples, which illustrates the effectiveness of Ag in enhancing the electrical conductivity of the catalyst. High-resolution TEM (HRTEM) image of the obtained P-SnO₂/Ag nanofibers in Fig. 1b reveals obviously porous nanostructures. The lattice spacing of lattice fringes are 0.33 nm and 0.24 nm, which well match the (110) plane of SnO₂ (JCPDS 41–1445) and (111) plane of Ag (JCPDS 99–0094), respectively (Fig. 1c). As shown in Fig. 1d, the EDX elemental mappings demonstrate the uniform distributions of the Sn, O and Ag elements. The crystallinity of the prepared catalysts is further characterized by XRD measurement. As shown in Fig. 1e, several main diffraction peaks at $2\theta = 26.6^\circ$, 33.9° , 37.9° , 51.8° , 54.8° , 62.6° and 65.9° are observed in the XRD pattern of P-SnO₂/Ag, which are indexed to the (110), (101), (200), (211), (220), (221) and (301) lattice planes of SnO₂ (JCPDS 41–1445), respectively [31]. While the diffraction peaks at $2\theta = 38.1^\circ$, 44.3° , 64.4° , and 77.4° are indexed to the (111), (200), (220), and (311) lattice planes of Ag (JCPDS 99–0094), respectively. The typical XRD peaks of P-SnO₂/Ag and SnO₂/Ag nanofibers get broader compared to those of P-SnO₂ nanofibers and P-Ag sample due to the growing of distortion zones between Ag and SnO₂ and grain refinement [32]. These results further verify the hybridized structure of P-SnO₂/Ag nanofibers. The chemical states and the electronic interactions around Ag and SnO₂ are further characterized by X-ray photoelectron spectroscopy (XPS) analysis. The XPS spectra of samples are calibrated with adventitious carbon with a characteristic peak located at 284.8 eV. The survey spectra of the typical samples are shown in Fig. S4, illustrating the presence of Sn, Ag and O elements in the P-SnO₂/Ag nanofibers. And the typical XPS fittings for Ag 3d, Sn 3d and O 1s spectra of the samples are shown in Figs. 1f, 1g and Fig. S5, respectively. The binding energies of Ag 3d are recorded at 374.2 and 368.2 eV ($\Delta E_g = 6.0$ eV) for P-Ag nanofibers, which can be assigned to the 3d_{3/2} and 3d_{5/2} peaks of Ag⁰, respectively [33]. And the Sn 3d spectrum of P-SnO₂ nanofibers exhibit two symmetrical characteristic peaks at 495.4 and 487.0 eV ($\Delta E_g = 8.4$ eV), which are corresponding to the Sn 3d_{3/2} and Sn 3d_{5/2} of Sn (IV) oxidation states, respectively [34]. However, a negative shift in the Ag 3d and Sn 3d are both observed in Figs. 1f and 1g for the P-SnO₂/Ag nanofibers compared to the corresponding components in P-Ag and P-SnO₂ nanofibers, respectively. This result suggests a charge transfer between the Ag and SnO₂ upon forming hybrid structure in the P-SnO₂/Ag nanofibers [32],

which might be beneficial to CO₂RR [35,36].

3.2. Electrochemical performances

The CO₂ electroreduction performances are investigated in a gas-tight H-cell with CO₂-saturated 0.5 M KHCO₃ electrolyte (pH = 7.3). The linear sweep voltammetry (LSV) measurement is firstly used to examine CO₂ electroreduction activity for all the samples from 0.2 to –1.8 V (vs. RHE) in CO₂ and N₂ saturated 0.5 M KHCO₃ electrolyte, respectively. As shown in Fig. 2a and Fig. S6, the onset potential (defined as the potential at which the total electrocatalytic current was 1 mA cm^{–2}) of P-SnO₂/Ag electrode is around at –0.56 V vs RHE, which is less than that of the solid SnO₂/Ag electrode (–0.57 V), P-SnO₂ electrode (–0.59 V) and P-Ag electrode (–0.64 V). Furthermore, P-SnO₂/Ag electrode exhibits the highest reduction current density among all the samples. The higher reduction current density of P-SnO₂/Ag electrode than SnO₂/Ag electrode indicates the formation of more active sites on the porous structure of P-SnO₂/Ag electrode [37]. At the same time, these current densities in CO₂-saturated electrolyte are obviously higher than these recorded in N₂-saturated electrolyte (pH=8) (Fig. S7), which mainly originates from the hydrogen evolution reaction (HER), indicating that the CO₂RR occurs readily [38]. According to the LSV results, it can be supposed that the continuous porous structure and the coupling of SnO₂ and Ag synergistically contribute to a high CO₂RR performances [37–39]. To quantify the activity and selectivity of the P-SnO₂/Ag electrode toward the CO₂RR, the electrochemical test is operated in a potentiostatic mode between –0.6 and –1.2 V (vs. RHE) in a typical H-type cell with CO₂-saturated electrolyte. The gas (CO, H₂) and liquid (HCOO[–]) products are quantitatively analyzed by online gas chromatograph (GC) and ¹H nuclear magnetic resonance (NMR) spectroscopy, respectively. As shown in Fig. S8, the calibration curve of formic acid concentration is obtained by analyzing the ¹H NMR testing results of 0.5 M KHCO₃ electrolyte with different concentrations of formic acid and a certain internal standard of DMSO. Fig. 2b reveals the Faradaic efficiency (FE) for HCOO[–], CO and H₂ of the P-SnO₂/Ag electrode during the CO₂RR and the total FEs of all these potentials are approaching 100%. It can be clearly observed that P-SnO₂/Ag electrode exhibits an outstanding electrocatalytic activity and selectivity to HCOO[–]. The FE of HCOO[–] production of P-SnO₂/Ag electrode is 62% at –0.6 V (vs. RHE) and increases gradually with the negative shift of potential. The maximum FE of 92.4% of HCOO[–] production is achieved at –0.9 V (vs. RHE), which is much higher than those of SnO₂/Ag electrode (52.3%) and P-SnO₂ electrode (34.4%) at the same potential, revealing the key roles of the porous structure and the coupling of SnO₂ and Ag on enhancing CO₂RR performance [40]. When the overpotential is further increased, the FE of HCOO[–] decreases, which may be caused by the limitation of mass transfer due to the limited solubility of CO₂ in aqueous electrolyte [41]. Remarkably, the total FEs of C1 products are higher than 80% during the testing voltage window of –0.8 to –1.2 V (vs. RHE). For P-Ag electrode, H₂ and CO are the dominant reduction products, and HCOO[–] is barely detected (Fig. S9), and the electrocatalytic results are consistent with typical Ag catalysts [42]. Furthermore, the partial current densities for C1 products of all the samples increase gradually as the potential negatively shifts. As shown in Fig. 2c, the P-SnO₂/Ag electrode exhibits a highest current density of 24.6 mA cm^{–2} at –0.9 V (vs. RHE), which is 1.5, 3.0, and 4.0 times as high as that of SnO₂/Ag electrode (16.5 mA cm^{–2}), P-SnO₂ electrode (8.0 mA cm^{–2}) and P-Ag electrode (6.4 mA cm^{–2}), respectively. Importantly, the outstanding CO₂RR performances comparable with the best Sn-based catalysts in H-type electrochemical cells (Table S1). In addition to the electrocatalytic activity and selectivity, electrochemical stability is also significant to evaluate an advanced electrocatalyst. As shown in Fig. 2d, the i-t curve is obtained by a long time chronoamperometry test at –0.9 V (vs. RHE). It is notable that the current density increases in the beginning 0.5 h electrolysis and maintains a current density of around 24 mA cm^{–2} for more than 10 h with a FE of

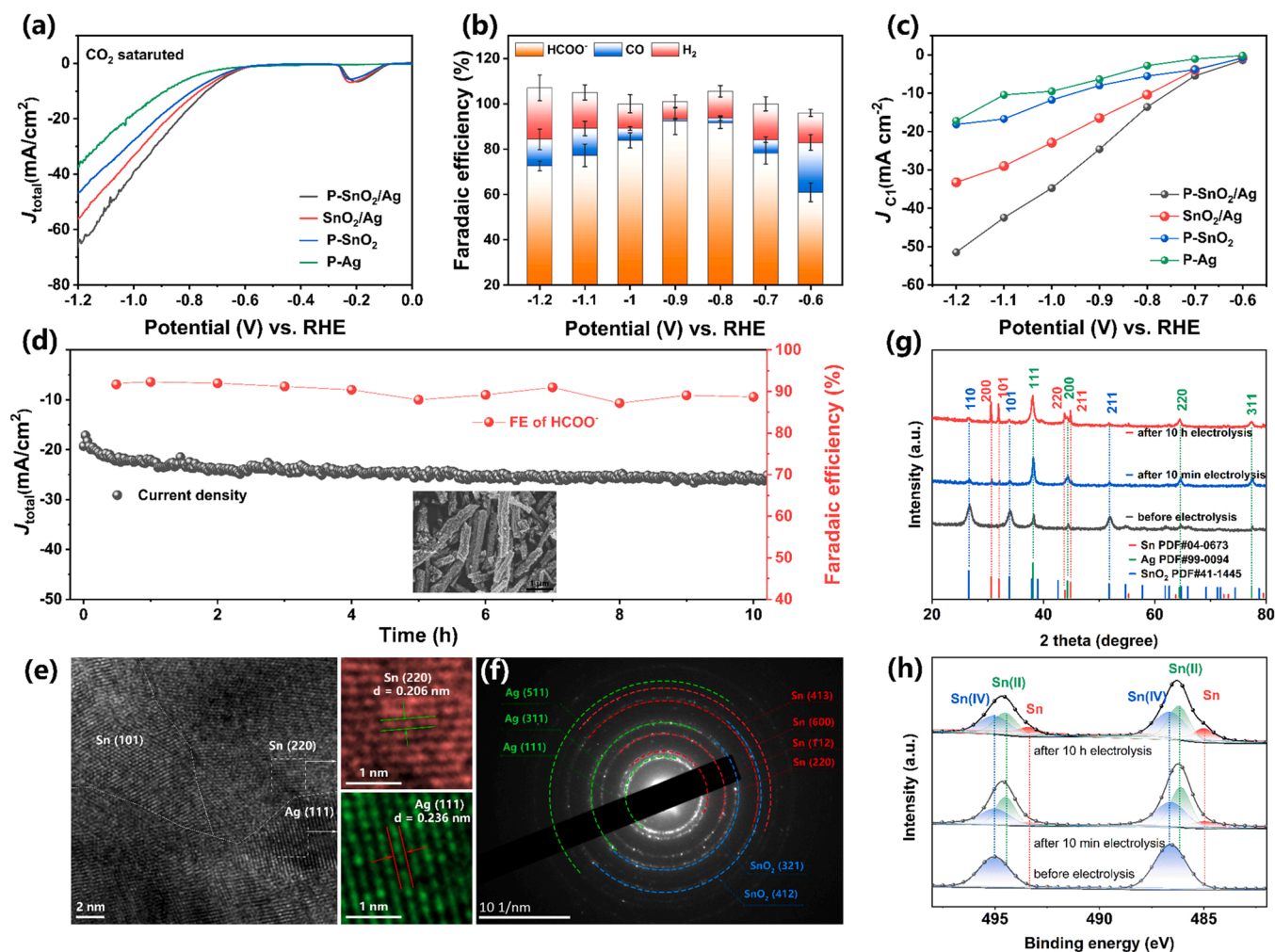


Fig. 2. (a) LSV curves of different electrodes in CO_2 saturated 0.5 M KHCO_3 . (b) FEs of HCOO^- , CO and H_2 for P- SnO_2/Ag electrode at varied potentials. (c) The partial current density for C1 product at potential ranging from -0.6 to -1.2 V (vs. RHE) with different electrodes. (d) Long-term stability of P- SnO_2/Ag electrode for CO_2RR at constant potential of -0.9 V (vs. RHE) for 10 h, the inset SEM image shows the morphology of the P- SnO_2/Ag after long-term stability test. (e) HRTEM image and (f) SAED pattern of P- SnO_2/Ag nanofibers after 10 h CO_2RR test at -0.9 V (vs. RHE). (g) XRD patterns and (h) typical Sn 3d XPS spectra of the P- SnO_2/Ag before (black) and after 10 min and 10 h CO_2RR test at -0.9 V (vs. RHE).

around 90% for HCOO^- . We also characterized the P- SnO_2/Ag electrode after a long-term stability test by SEM, TEM, HRTEM and ICP measurement. As shown in the inset of Fig. 2d and Fig. S10, the P- SnO_2/Ag nanofibers still exhibit a porous nanofiber structure, and both Ag and Sn are uniformly distributed on their surface. ICP result shows that the relative contents of Ag and Sn hardly change before and after the long-term stability test, further confirming the robust stability of P- SnO_2/Ag nanofibers (Fig. S11). High-resolution transmission electron microscopy (HRTEM) images and selected area electron diffraction (SAED) patterns are obtained to investigate the crystal structure of P- SnO_2/Ag nanofibers after electrolysis. The HRTEM image presents well-defined crystal plane spacings of 0.206 and 0.236 nm (Fig. 2e), which well match the (220) plane of Sn (JCPDS 04-0673) and (111) plane of Ag (JCPDS 99-0094), respectively [43]. The diffraction rings in the SAED pattern further prove the existence of metallic Sn, and the appearance of the diffraction rings attributed to SnO_2 might be related to the partial oxidation of the metallic Sn on its surface (Fig. 2f). All these results indicate that the tin dioxide in P- SnO_2/Ag nanofibers can be reduced to the metallic Sn after undergoing the electrolytic experiments, which may play an important role in the catalytic process.

XRD patterns and XPS spectra are further used to investigate the crystal structure and valence states of surface species of P- SnO_2/Ag nanofibers electrolyzed at different times to further reveal the real

catalytic active sites [13]. In order to minimize the oxidation of metal tin in the air, the working electrode was quickly taken out, rinsed with deionized water and dried with nitrogen, sealed and stored in a centrifuge tube filled with nitrogen, and XRD and XPS test were carried out within 30 min after the electrocatalytic experiment [44]. As shown in Fig. 2g, after 10 min of electrolysis, the diffraction peaks at $2\theta = 26.6^\circ$, 33.9° , 37.9° belonging to the (110), (101) and (200) lattice planes of SnO_2 , respectively (JCPDS 41-1445) are significantly reduced [43]. And several new diffraction peaks appear at $2\theta = 30.6^\circ$, 32.0° , 43.9° and 44.9° , indexed to the (200), (101), (220) and (211) lattice planes of Sn, respectively (JCPDS 04-0673) [43]. As the electrolysis time is extended to 10 h, the diffraction peaks of Sn are dominated in the XRD pattern, and the diffraction peaks of Ag ($2\theta = 38.1^\circ$, 44.3° , 64.4° , and 77.4° (JCPDS 99-0094)) do not change significantly during the whole process. These results indicated that SnO_2 in P- SnO_2/Ag nanofibers are easily reduced to metallic tin during the electrolytic process. The coexistence of the weak SnO_2 diffraction peaks might be due to the existence of the partially unreduced SnO_2 and the easy oxidation of Sn exposed to air during the test. However, it is generally considered that the specific active sites on the surface of catalyst usually contributes to the electrocatalytic activity [24], thus it is necessary to study the formed species on the surface of catalyst to reveal the electrocatalytic mechanism. As shown in the typical Sn 3d XPS spectra of the P- SnO_2/Ag before and after

CO₂RR test at -0.9 V (vs. RHE) (Fig. 2 h), the appearances of peaks at 493.4 and 485.0 eV are mainly fitted to metallic Sn 3d_{3/2} and 3d_{5/2} after 10 min of electrolysis [45,46]. Further prolonging the electrolysis time, the characteristic peaks of metallic Sn gradually become stronger, while there are still some weak characteristic peaks corresponding to the oxidized species (Sn (II) and/or Sn (IV)) [13,34]. The XPS results demonstrate the existence of metallic Sn on the surface of P-SnO₂/Ag nanofibers after electrolysis, even if the sample is inevitably exposed to air, which provides support for metallic tin to be the true active site. However, to avoid catalyst evolution in non-catalytic environments, it is necessary to perform in-situ tests, such as in-situ electrochemical-Raman spectra [13,16,22,23].

Based on the above discussions, we reasonably speculate the excellent CO₂RR activity and superior HCOO⁻ selectivity of the P-SnO₂/Ag electrode may be attributed to the synergistic effect from the following three aspects. Firstly, abundant exposing active sites from the porous structure facilitate the activation of CO₂ molecules [47] and enable remarkable electrocatalytic performance [48]. Secondly, the improved electrical conductivity of the P-SnO₂/Ag electrode facilitates the electron transfer from the electrode to the reactants, which favors the formation of *CO₂ intermediate [39,49]. Finally, the formation of a heterostructure between SnO₂ and Ag facilitates the electron transfer from Ag to Sn, resulting in easier reduction of SnO₂ at the reduction potential, which is beneficial to optimize the specific reaction intermediates and improve its selective catalytic ability and inhibit the hydrogen evolution reaction [50].

To verify our interpretation of the superior catalytic performance and selectivity of P-SnO₂/Ag electrode, we further evaluate the electrochemically active surface area (ECSA) from double-layer capacitance values (C_{dl}) determined by CV measurement at different scan rates in non-Faradaic region (Fig. S13). As shown in Fig. 3a, the capacitance of

P-SnO₂/Ag electrode is highest (11.55 mF cm⁻²), in comparison with that of SnO₂/Ag electrode (6.42 mF cm⁻²), P-SnO₂ electrode (5.52 mF cm⁻²) and P-Ag electrode (4.95 mF cm⁻²). The increased C_{dl} of P-SnO₂/Ag electrode is likely due to its large porosity [37,51,52] and the synergistically coupling effect of SnO₂ and Ag [35,53], which provide augmented catalytically active sites during CO₂RR process. Electrochemical impedance spectroscopy (EIS) measurements are also performed in a CO₂-saturated 0.5 M KHCO₃ solution at a constant potential of -1.2 V (vs. RHE) to understand the electron transfer process of the CO₂RR. The Nyquist plots of all the electrodes are shown in Fig. 3b and fitted by the equivalent circuit (Fig. 3b insert). The high frequency intercept and the diameter of the semicircular Nyquist plot reflect the ohmic resistance (R_{ohm}) and the charge-transfer resistance (R_{ct}), respectively. The R_{ct} of P-SnO₂/Ag electrode (30.1 Ω) is smaller than that of SnO₂/Ag electrode (35.1 Ω), P-SnO₂ electrode (44.8 Ω) and P-Ag electrode (42.6 Ω), demonstrating that P-SnO₂/Ag electrode exhibits the most favorable kinetics of the charge transfer process between the electrode and the electron acceptor in the CO₂RR, which is resulting from the abundant active sites and the favorable surface properties [47, 54]. To further investigate the reaction kinetics for CO₂RR, Tafel plots are obtained based on j_{HCOO^-} at various overpotentials. As shown in Fig. 3c, in contrast with the Tafel slope of 199 and 246 mV dec⁻¹ for SnO₂/Ag electrode and P-SnO₂ electrode, respectively, the lowest Tafel slope of P-SnO₂/Ag electrode of 144 mV dec⁻¹ is obtained, indicating the boosted reaction kinetics of CO₂RR to HCOO⁻ on P-SnO₂/Ag electrode [55]. The Tafel slope value of the P-SnO₂/Ag electrode implies that the formation of *CO₂ via the adsorption of CO₂ with concomitant electron transfer (ET) step would be the rate-limiting step in the electrochemical reduction of CO₂ to HCOO⁻ reaction [56,57]. On the other hand, for CO production, the Tafel slope of P-Ag electrode (166 mV dec⁻¹) in Fig. S14 indicates the production *CO₂ is the rate-limiting step,

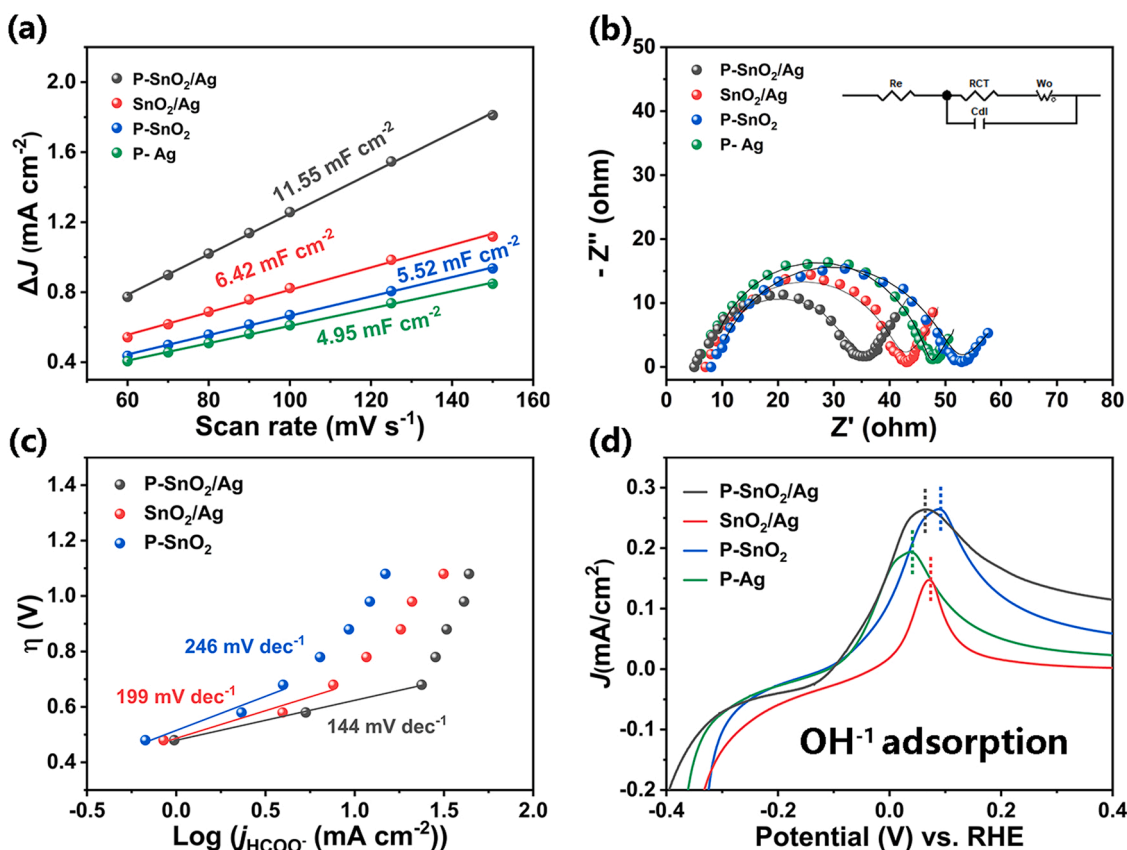


Fig. 3. (a) Double layer capacitance of all electrodes for ECSA evaluation, half of charging current density differences ($D_{j/2}$) are plotted against scan rates. (b) Nyquist plots for the different electrodes with corresponding equivalent circuit. (c) Tafel plots of the HCOO⁻ for different electrodes. (d) OH⁻ adsorption affinities on different electrodes.

too [55]. The properties and states of $^*\text{CO}_2$ intermediate on the catalyst surface would directly affect the subsequent reaction pathway. We further explore the adsorption capacity of the $^*\text{CO}_2$ intermediate on the catalyst surface by the single oxidative LSV scans in a N_2 saturated 1.0 M KOH solution [47,58]. As shown in Fig. 3d, the oxidative adsorption potential of OH^- surrogate ions on the P-Ag electrode is around 24 mV, which is more negative than that on the P-SnO₂/Ag electrode, indicating that the adsorption capacity of $^*\text{CO}_2$ intermediate is stronger on P-Ag electrode than the latter. On the one hand, the improved adsorption affinity of $^*\text{CO}_2$ suggests that the easier generation of $^*\text{CO}_2$ via the electron transfer step, often at the expense of the increase of the barrier to further reduction and protonation of $^*\text{CO}_2$ [58]. On the other hand, too weak adsorption is not conducive to the activation of the reactants on the electrode. Experimentally, the catalytic activity and selectivity of P-SnO₂/Ag electrode would be maximized by the optimization of the adsorption affinity of $^*\text{CO}_2$ [59].

3.3. In-situ SERS spectra

To determine the mechanism of the enhanced CO₂RR performance of P-SnO₂/Ag electrode, an in-situ electrochemical SERS measurement device (Fig. 4a and Scheme S2) is carried out to track the evolution of catalysts and investigate the possible reaction intermediates during CO₂RR. We first used *p*-aminothiophenol (PATP) as probe molecules to evaluate the SERS performance of P-SnO₂/Ag. As shown in Fig. S15, the signals of characteristic peaks can still be detected even the concentration of PATP reduces to 10^{-10} M, suggesting the excellent SERS behavior of the P-SnO₂/Ag nanofibers. Therefore, it is possible to provide a powerful in-situ and real-time monitoring technique to collect information on the reaction intermediates and local reaction environment for the electrocatalytic CO₂RR. Furthermore, with this unique SERS information in detail, it is possible to monitor the reaction process and reveal the reaction mechanism under experimental conditions [59].

As shown in Fig. 4b and c, the Raman spectra of both the P-SnO₂/Ag and P-SnO₂ electrode show the characteristic Raman peaks at 632 cm^{-1} at open circuit potential (OCP), which is assigned to A_{1g} mode of the SnO₂ [60,61]. Clearly, when the applied potential shifts negatively to -0.175 V (vs. RHE), the intensity of this Raman peak decreases rapidly for the P-SnO₂/Ag electrode, while some distinct peaks appear at 606, 288 and 248 cm^{-1} , corresponding to the reduction of SnO₂ to lower oxidation states (Table S2) [13,62–65]. As the potential shifts negatively further, these peaks of this tin oxidation states gradually decrease and disappear almost completely at -0.375 V (vs. RHE), suggesting the

further reduction of oxidized Sn to metallic Sn. At the same time, P-SnO₂/Ag exhibits an excellent SERS performance, significantly enhancing the signals at 288 and 248 cm^{-1} , and some peaks belonging to tin oxides in the range of $400\text{--}600\text{ cm}^{-1}$ are also detected [60,61]. In contrast, for P-SnO₂ electrode, although this similar potential-dependent behavior still exists, the A_{1g} peak corresponding to SnO₂ decreases more slowly, and a relatively broad Raman peak can still be observed until -0.475 V (vs. RHE) (Fig. 4c). And when the applied potential shifts negatively to -0.575 V (vs. RHE), these peaks of tin oxidation states become barely visible. The in-situ SERS spectroscopy provides strong evidence that metallic tin likely be the real active site on P-SnO₂/Ag and P-SnO₂ electrode rather than Sn (IV) and Sn (II) oxide species during CO₂ reduction (-0.6 V), which is consistent with previous findings [13]. By plotting the normalized peak area of the A_{1g} peak in the spectra as a function of the applied potential, as shown in Fig. S16, it can be clearly found that P-SnO₂/Ag is more easily reduced than P-SnO₂ electrode. This is likely because in P-SnO₂/Ag electrode, the electron transfer from Ag to SnO₂ leads to a decrease in the oxidation state of Sn, which is also confirmed by the XPS results in Fig. 1g [35].

To further understand the mechanism of the enhanced selectivity for HCOO[−] on the P-SnO₂/Ag electrode, more information about the reaction process is needed, especially the signals of the reaction intermediates. For comparison, we have also studied the in-situ SERS spectra of P-Ag electrode in the electrochemical process, which exhibits good selectivity toward CO production. Fig. 5a and b exhibit the in-situ SERS spectra of the P-SnO₂/Ag and P-Ag electrodes, respectively, which are obtained in a specially designed electrolysis cell with a CO₂-saturated 0.5 M KHCO₃ aqueous solution at different applied potential. As shown in Fig. 5a, no signals are detected under open circuit potential (OCP), and two distinct Raman bands at 1340 and 1540 cm^{-1} appear when the applied potential shifts negatively to -0.4 V (vs. RHE), which can be ascribed to the symmetric stretching and asymmetric stretching vibrations of $^*\text{CO}_2$ intermediate, respectively [16,66]. As the potential shifts negatively further, the intensity of the $^*\text{CO}_2$ intermediate peak increases and reaches a maximum at -0.8 V (vs. RHE) and then drops gradually, which suggests that $^*\text{CO}_2$ intermediate is very favorably involved in further transformations. At the same time, peak at 1540 cm^{-1} gradually shifts to 1570 cm^{-1} as the potential decreases, which may be due to the change of the adsorption configuration of $^*\text{CO}_2$ intermediate on the surface of P-SnO₂/Ag electrode [67,68]. More importantly, a broad peak at 1420 cm^{-1} is detected at the potential range between -0.4 and -1.2 V (vs. RHE) and assigned to O-(CH)-O stretching of $^*\text{OCHO}^*$ [67]. As shown in the right figure in Fig. 5a, it can

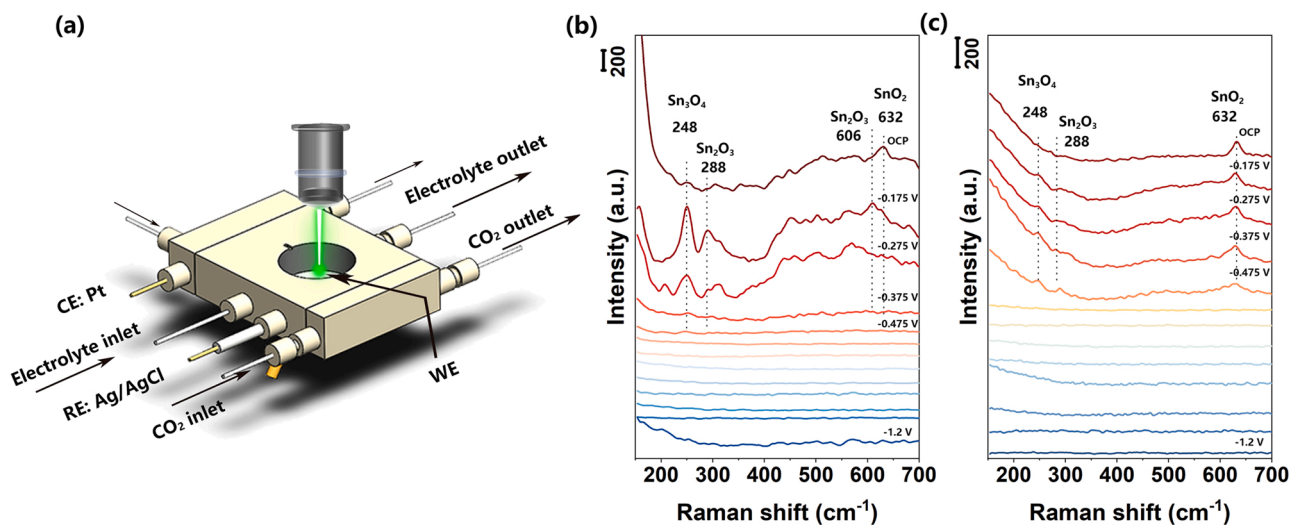


Fig. 4. (a) In-situ electrochemical SERS measurement device and in-situ SERS spectra of CO₂RR on (b) P-SnO₂/Ag and (c) P-SnO₂ electrode at different potentials in 0.5 M KHCO₃ solution saturated with CO₂.

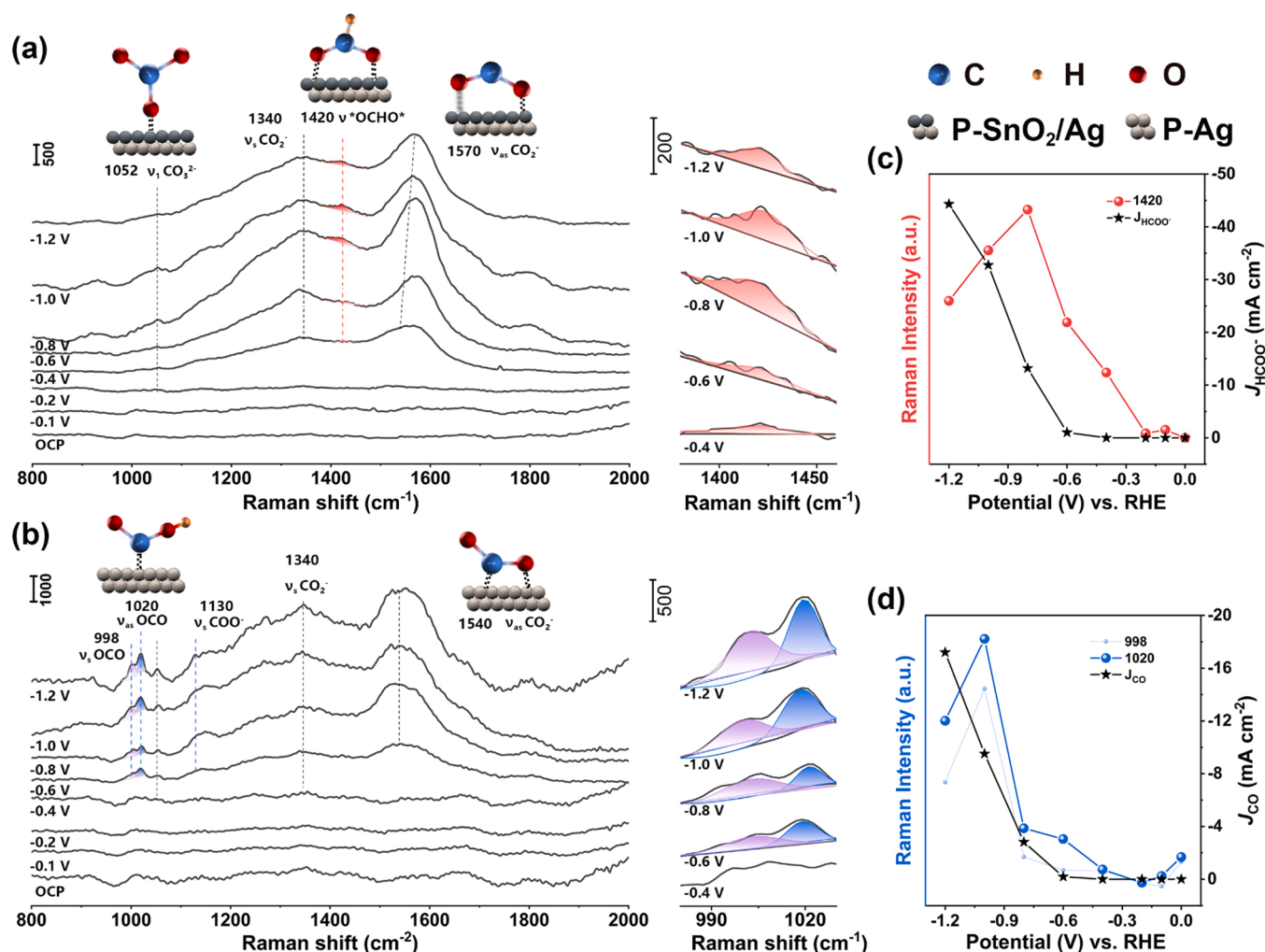


Fig. 5. In-situ SERS spectra of CO₂RR on (a) P-SnO₂/Ag and (b) P-Ag electrode at different potentials in 0.5 M KHCO₃ solution saturated with CO₂. (c) The Raman intensities of *OCHO* peak and current densities for HCOO⁻ on P-SnO₂/Ag electrode at different applied potentials. (d) The Raman intensities of *COOH peak and current densities for CO on P-Ag electrode at different applied potentials.

be clearly seen that the Raman peak at 1420 cm⁻¹ appears at -0.4 V (vs. RHE), gradually increases with the negative shift of the potential, and then gradually weakens after reaching the strongest at -0.8 V (vs. RHE). Similar trends are also found in many in-situ electrocatalytic spectroscopy studies, which are generally resulting from the accumulation and rapid consumption of reaction intermediates [23,69–73]. In order to verify the reliability of the data, we have used P-SnO₂/Ag nanofibers prepared in different batches as catalysts to be performed in-situ electrochemical SERS experiments at a voltage of -0.9 V (vs. RHE). As shown in Fig. S17a, the characteristic peak at 1420 cm⁻¹ can be monitored by collecting the spectra at different times in three batch experiments. The relative standard deviation (RSD) of the characteristic peak of 1420 cm⁻¹ in nine spectra is calculated to be 10.25%, indicating that *OCHO* intermediate plays a stable and necessary role for HCOO⁻ production (Fig. S17b). This provides a direct spectroscopic evidence for the chemisorption of *OCHO* on the surface of P-SnO₂/Ag electrode via two oxygen atoms, which is widely believed to be a key intermediate for the formation of HCOO⁻ [74]. However, the appearance of 1340 and 1540 cm⁻¹ peaks are observed at a more negative potential (-0.5 V vs. RHE) on P-Ag electrode (Fig. 5b), indicating the blocked formation of the surface-absorbed *CO₂ intermediate on P-Ag electrode than that on P-SnO₂/Ag electrode. Unlike P-SnO₂/Ag electrode, the intensity of the peak at 1540 cm⁻¹ gradually increases as the potential decreases further, implying that *CO₂ intermediate is accumulating rather than

actively participating in further reactions (Fig. S18). On the other hand, two peaks at 998 and 1020 cm⁻¹ appear when the potential reaches -0.7 V (vs. RHE) in Fig. 5b, which may be derived from *COOH vibration [74,75]. While *COOH is widely regarded as a key intermediate in the formation of CO during CO₂RR [76,77].

To better understand the reaction intermediates and the selectivity of catalysts, we calculate the intensities of characteristic peaks and current densities of CO₂RR products as a function of applied potential [78]. As shown in Fig. 5c and d, the selectivity of the P-SnO₂/Ag electrode and P-Ag electrode for HCOO⁻ and CO production has a good correspondence with *OCHO* and *COOH, respectively. And the decrease in the intensity of the characteristic peaks at large potentials might be due to the limitation of CO₂ mass transfer.

Combining the electrochemical test with in-situ SERS experiment, the catalytic mechanism of P-SnO₂/Ag electrode and P-Ag electrode toward CO₂RR can be described as Fig. 6: Firstly, the CO₂ molecules in the electrolyte takes an electron from the electrode to form a *CO₂ intermediate, which is the rate-limiting step for both HCOO⁻ and CO production [79]. Then, the next reaction step is largely related to the adsorption affinity with *CO₂ intermediate on the electrode surface. On the one hand, when *CO₂ is suitable adsorbed on the electrode, the protons from electrolyte will react favorably with O atom of *CO₂ to form *OCHO* intermediate and further HCOO⁻ [79]. On the other hand, when the *CO₂ is adsorbed on the electrode via C atom due to strong

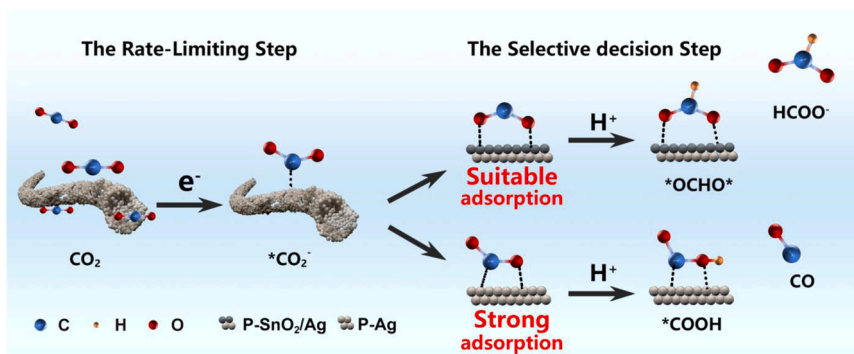


Fig. 6. Schematic representation of the CO₂RR pathway for HCOO[−] and CO production resulting from different absorption affinity.

adsorption affinity, the protons may easily react with the O atom with extra electron density, forming *COOH intermediate. Finally, *OCHO* and *COOH intermediates further react with e[−] and H⁺ to produce HCOO[−] and CO, respectively [79].

4. Conclusions

In summary, P-SnO₂/Ag nanofibers are successfully prepared via an electrospinning and subsequent two-step calcination process to display superior electrocatalytic performance toward CO₂RR with a large catalytic activity, high selectivity and desirable stability due to the synergistic effect of the porous structure and the coupling effect between SnO₂ and Ag component. Combining in-situ SERS spectra and X-ray diffraction (XRD) patterns indicates that that metallic tin likely be the real active site rather than Sn (IV) and Sn (II) oxide species in CO₂ electroreduction to formate. Furthermore, the inherent SERS property of the P-SnO₂/Ag nanofibers enables in-situ and real-time acquisition of specific signals for key *OCHO* intermediate to produce HCOO[−], which is beneficial to achieve the excellent selectivity of P-SnO₂/Ag nanofibers. Overall, this work directly demonstrates the effectiveness of optimizing catalytic selectivity by regulating the adsorption of catalysts to reaction intermediates. And presents a promising strategy to optimize catalytic performance by simultaneously manipulation of the structure and compositions of the metal oxide/metal hybrids, while endowing the catalysts with multifunctionality to reveal the reaction mechanism.

CRediT authorship contribution statement

Junjie Chen: Investigation, Data curation, Formal analysis, Writing – original draft. **Benhua Ma:** Methodology, Instrument. **Zhoubing Xie:** Methodology, Software, Instrument. **Weimo Li:** Methodology, Software, Instrument. **Yumei Yang:** Data curation, Formal analysis. **Ming Mu:** Data curation, Formal analysis. **Xiaoxin Zou:** Methodology, Software, Instrument. **Bing Zhao:** Supervision, Investigation, Methodology. **Wei Song:** Supervision, Methodology, Visualization, Investigation, Writing – review & editing.

Declaration of Competing Interest

The authors declare the following financial interests/personal relationships which may be considered as potential competing interests: Wei Song reports financial support was provided by National Natural Science Foundation of China.

Data availability

Data will be made available on request.

Acknowledgements

This work was supported by the research grants from the National Natural Science Foundation of China (22074051, 92161119) and the Open Funds of State Key Laboratory of Inorganic Synthesis and Preparative Chemistry (2023-7).

Supporting Information

Experimental apparatus and procedure, catalyst characterization and additional results of Structural characterization.

Appendix A. Supporting information

Supplementary data associated with this article can be found in the online version at doi:10.1016/j.apcatb.2022.122350.

References

- [1] K. Zickfeld, A.H. MacDougall, H.D. Matthews, On the proportionality between global temperature change and cumulative CO₂ emissions during periods of net negative CO₂ emissions, *Environ. Res. Lett.* 11 (2016), 055006.
- [2] D.R. Feldman, W.D. Collins, P.J. Gero, M.S. Torn, E.J. Mlawer, T.R. Shippert, Observational determination of surface radiative forcing by CO₂ from 2000 to 2010, *Nature* 519 (2015) 339–343.
- [3] A.M. Appel, J.E. Bercaw, A.B. Bocarsly, H. Dobbek, D.L. DuBois, M. Dupuis, J. G. Ferry, E. Fujita, R. Hille, P.J. Kenis, C.A. Kerfeld, R.H. Morris, C.H. Peden, A. R. Portis, S.W. Ragsdale, T.B. Rauchfuss, J.N. Reek, L.C. Seefeldt, R.K. Thauer, G. L. Waldrop, Frontiers, opportunities, and challenges in biochemical and chemical catalysis of CO₂ fixation, *Chem. Rev.* 113 (2013) 6621–6658.
- [4] M.G. Kibria, J.P. Edwards, C.M. Gabardo, C.T. Dinh, A. Seifitokaldani, D. Sinton, E. H. Sargent, Electrochemical CO₂ reduction into chemical feedstocks: from mechanistic electrocatalysis models to system design, *Adv. Mater.* 31 (2019), e1807166.
- [5] C. Xia, P. Zhu, Q. Jiang, Y. Pan, W. Liang, E. Stavitski, H.N. Alsharief, H. Wang, Continuous production of pure liquid fuel solutions via electrocatalytic CO₂ reduction using Solid-electrolyte devices, *Nat. Energy* 4 (2019) 776–785.
- [6] K. Deng, Y. Zhang, H. Feng, N. Liu, L. Ma, J. Duan, Y. Wang, D. Liu, Q. Li, Efficient solar fuel production with a high-pressure CO₂-captured liquid feed, *Sci. Bull.* 67 (2022) 1467–1476.
- [7] S.-F. Tang, X.-L. Lu, C. Zhang, Z.-W. Wei, R. Si, T.-B. Lu, Decorating graphdiyne on ultrathin bismuth subcarbonate nanosheets to promote CO₂ electroreduction to formate, *Sci. Bull.* 66 (2021) 1533–1541.
- [8] F. Ren, W. Hu, C. Wang, P. Wang, W. Li, C. Wu, Y. Yao, W. Luo, Z. Zou, An extrinsic faradaic layer on CuSn for high-performance electrocatalytic CO₂ reduction, *CCS Chem.* 4 (2022) 1610–1618.
- [9] S. Zhao, S. Li, T. Guo, S. Zhang, J. Wang, Y. Wu, Y. Chen, Advances in Sn-based catalysts for electrochemical CO₂ reduction, *Nano-Micro Lett.* 11 (2019) 62.
- [10] X. Zu, X. Li, W. Liu, Y. Sun, J. Xu, T. Yao, W. Yan, S. Gao, C. Wang, S. Wei, Y. Xie, Efficient and robust carbon dioxide electroreduction enabled by atomically dispersed Sn⁰ Sites, *Adv. Mater.* 31 (2019), e1808135.
- [11] Z. Chen, T. Fan, Y.-Q. Zhang, J. Xiao, M. Gao, N. Duan, J. Zhang, J. Li, Q. Liu, X. Yi, J.-L. Luo, Wavy SnO₂ catalyzed simultaneous reinforcement of carbon dioxide adsorption and activation towards electrochemical conversion of CO₂ to HCOOH, *Appl. Catal. B* 261 (2020), 118243.
- [12] Z. Chen, M.-R. Gao, N. Duan, J. Zhang, Y.-Q. Zhang, T. Fan, J. Zhang, Y. Dong, J. Li, Q. Liu, X. Yi, J.-L. Luo, Tuning adsorption strength of CO₂ and its intermediates on tin oxide-based electrocatalyst for efficient CO₂ reduction towards carbonaceous products, *Appl. Catal. B* 277 (2020), 119252.

- [13] M. He, B. Xu, Q. Lu, Probing the role of surface speciation of tin oxide and tin catalysts on CO₂ electroreduction combining in situ Raman spectroscopy and reactivity investigations, *Chin. J. Catal.* 43 (2022) 1473–1477.
- [14] Q. Li, J. Fu, W. Zhu, Z. Chen, B. Shen, L. Wu, Z. Xi, T. Wang, G. Lu, J.J. Zhu, S. Sun, Tuning Sn-catalysis for electrochemical reduction of CO₂ to CO via the core/shell Cu/SnO₂ structure, *J. Am. Chem. Soc.* 139 (2017) 4290–4293.
- [15] Y. Zhao, X. Liu, Z. Liu, X. Lin, J. Lan, Y. Zhang, Y.R. Lu, M. Peng, T.S. Chan, Y. Tan, Spontaneously Sn-doped Bi/BiOx core-shell nanowires toward high-performance CO₂ electroreduction to liquid fuel, *Nano Lett.* 21 (2021) 6907–6913.
- [16] I.V. Chernyshova, P. Somasundaran, S. Ponnuram, On the origin of the elusive first intermediate of CO₂ electroreduction, *Proc. Natl. Acad. Sci. USA* 115 (2018) E9261–E9270.
- [17] L.P.L. Gonçalves, J. Mielby, O.S.G.P. Soares, J.P.S. Sousa, D.Y. Petrovych, O. I. Lebedev, M.F.R. Pereira, S. Kegnas, Y.V. Kolen'ko, In situ investigation of the CO₂ methanation on carbon/ceria-supported Ni catalysts using modulation-excitation DRIFTS, *Appl. Catal. B* 312 (2022).
- [18] H.-L. Liu, K. Zhan, K. Wang, X.-H. Xia, Nanopore-based surface-enhanced Raman scattering technologies, *Sci. Bull.* 67 (2022) 1539–1541.
- [19] S. Wen, X. Ma, H. Liu, G. Chen, H. Wang, G. Deng, Y. Zhang, W. Song, B. Zhao, Y. Ozaki, Accurate monitoring platform for the surface catalysis of nanozyme validated by surface-enhanced Raman-kinetics model, *Anal. Chem.* 92 (2020) 11763–11770.
- [20] Q. Zhao, W. Song, B. Zhao, B. Yang, Spectroscopic studies of the optical properties of carbon dots: recent advances and future prospects, *Mater. Chem. Front.* 4 (2020) 472–488.
- [21] M. Mu, S.S. Wen, S.Z. Hu, B. Zhao, W. Song, Putting surface-enhanced Raman spectroscopy to work for nanozyme research: methods, materials and applications, *TrAC Trends Anal. Chem.* 152 (2022), e2002435.
- [22] Y. Ichinohe, T. Wadayama, A. Hatta, Electrochemical reduction of CO₂ on silver as probed by surface-enhanced Raman scattering, *J. Raman Spectrosc.* 26 (1995) 335–340.
- [23] Y. Zhao, X.-G. Zhang, B. Nataraju, W. Yang, Q. Liang, P. Radjenovic, Y.-H. Wang, Y.-J. Zhang, J.-C. Dong, Z.-Q. Tian, J.-F. Li, Elucidating electrochemical CO₂ reduction reaction processes on Cu(hkl) single-crystal surfaces by in situ Raman spectroscopy, *Energy Environ. Sci.* 15 (2022) 3968–3977.
- [24] H. Chen, X. Liang, Y. Liu, X. Ai, T. Asefa, X. Zou, Active site engineering in porous electrocatalysts, *Adv. Mater.* 32 (2020), e2002435.
- [25] F. Li, L. Chen, G.P. Knowles, D.R. MacFarlane, J. Zhang, Hierarchical mesoporous SnO₂ nanosheets on carbon cloth: a robust and flexible electrocatalyst for CO₂ reduction with high efficiency and selectivity, *Angew. Chem. Int. Ed.* 56 (2017) 505–509.
- [26] R. Hesamoddin, G. Lei, Z. Xueqin, H. Shihui, L. Mengran, S. Simon, Z. Zhonghua, W. Hao, Y. Zhiguo, Stand-alone asymmetric hollow fiber gas-diffusion electrodes with distinguished bronze phases for high-efficiency CO₂ electrochemical reduction, *Appl. Catal. B* 298 (2021), 120538.
- [27] G. Liu, Z. Li, J. Shi, K. Sun, Y. Ji, Z. Wang, Y. Qiu, Y. Liu, Z. Wang, P. Hu, Black reduced porous SnO₂ nanosheets for CO₂ electroreduction with high formate selectivity and low overpotential, *Appl. Catal. B* 260 (2020), 118134.
- [28] J.-S. Jang, S.-J. Choi, S.-J. Kim, M. Hakim, L.-D. Kim, Rational design of highly porous SnO₂ nanotubes functionalized with biomimetic nanocatalysts for direct observation of simulated diabetes, *Adv. Funct. Mater.* 26 (2016) 4740–4748.
- [29] J.G. Partridge, M.R. Field, J.L. Peng, A.Z. Sadek, K. Kalantar-Zadeh, J. Du Plessis, D.G. McCulloch, Nanostructured SnO₂ films prepared from evaporated Sn and their application as gas sensors, *Nanotechnology* 19 (2008), 125504.
- [30] Q. Wang, C. Li, J. Bai, J. Wang, Synthesis of Ag porous carbon nanofiber by electrospinning and their use as catalyst for styrene epoxidation, *Synth. React. Inorg. Met. Org. Nano-Met. Chem.* 46 (2016) 1773–1778.
- [31] D. Li, L. Huang, Y. Tian, T. Liu, L. Zhen, Y. Feng, Facile synthesis of porous Cu-Sn alloy electrode with prior selectivity of formate in a wide potential range for CO₂ electrochemical reduction, *Appl. Catal. B* 292 (2021), 120119.
- [32] S.K. Rai, A. Kumar, V. Shankar, T. Jayakumar, K. Bhanu Sankara Rao, B. Raj, Characterization of microstructures in Inconel 625 using X-ray diffraction peak broadening and lattice parameter measurements, *Scr. Mater.* 51 (2004) 59–63.
- [33] K. Maity, D.K. Panda, E. Lochner, S. Saha, Fluoride-induced reduction of Ag(I) cation leading to formation of silver mirrors and luminescent Ag-nanoparticles, *J. Am. Chem. Soc.* 137 (2015) 2812–2815.
- [34] R.G. Motsoeneng, I. Kortidis, S.S. Ray, D.E. Motaung, Designing SnO₂ nanostructure-based sensors with tailored selectivity toward propanol and ethanol vapors, *ACS Omega* 4 (2019) 13696–13709.
- [35] Z. Cai, Y. Wu, Z. Wu, L. Yin, Z. Weng, Y. Zhong, W. Xu, X. Sun, H. Wang, Unlocking bifunctional electrocatalytic activity for CO₂ reduction reaction by win-win metal-oxide cooperation, *ACS Sustain. Lett.* 3 (2018) 2816–2822.
- [36] A. Vasileff, X. Zhi, C. Xu, L. Ge, Y. Jiao, Y. Zheng, S.-Z. Qiao, Selectivity control for electrochemical CO₂ reduction by charge redistribution on the surface of copper alloys, *ACS Catal.* 9 (2019) 9411–9417.
- [37] D. Tan, W. Lee, Y.E. Kim, Y.N. Ko, M.H. Youn, Y.E. Jeon, J. Hong, S.K. Jeong, K. T. Park, SnO₂/ZnO composite hollow nanofiber electrocatalyst for efficient CO₂ reduction to formate, *ACS Sustain. Chem. Eng.* (2020) 10639–10645.
- [38] J. Zhang, M. Qiao, Y. Li, Q. Shao, X. Huang, Highly active and selective electrocatalytic CO₂ conversion enabled by core/shell Ag/(amorphous-Sn(IV)) nanostructures with tunable shell thickness, *ACS Appl. Mater. Interfaces* 11 (2019) 39722–39727.
- [39] M. Li, Y. Hu, D. Wang, D. Geng, Enhanced electrochemical reduction of CO₂ to CO on Ag/SnO₂ by a synergistic effect of morphology and structural defects, *Chem. Asian J.* 16 (2021) 2694–2701.
- [40] Y. Fu, T. Wang, W. Zheng, C. Lei, B. Yang, J. Chen, Z. Li, L. Lei, C. Yuan, Y. Hou, Nanoconfined Tin oxide within N-doped nanocarbon supported on electrochemically exfoliated graphene for efficient electroreduction of CO₂ to formate and C1 products, *ACS Appl. Mater. Interfaces* 12 (2020) 16178–16185.
- [41] Y.C. Tan, K.B. Lee, H. Song, J. Oh, Modulating local CO₂ concentration as a general strategy for enhancing C–C coupling in CO₂ electroreduction, *Joule* 4 (2020) 1104–1120.
- [42] C. Kim, H.S. Jeon, T. Eom, M.S. Jee, H. Kim, C.M. Friend, B.K. Min, Y.J. Hwang, Achieving selective and efficient electrocatalytic activity for CO₂ reduction using immobilized Silver nanoparticles, *J. Am. Chem. Soc.* 137 (2015) 13844–13850.
- [43] B. Ren, Z. Zhang, G. Wen, X. Zhang, M. Xu, Y. Weng, Y. Nie, H. Dou, Y. Jiang, Y. P. Deng, G. Sun, D. Luo, L. Shui, X. Wang, M. Peng, A. Yu, Z. Chen, Dual-Scale integration design of Sn-ZnO catalyst toward efficient and stable CO₂ electroreduction, *Adv. Mater.* 34 (2022), e2204637.
- [44] T.D. Nguyen-Phan, L. Hu, B.H. Howard, W. Xu, E. Stavitski, D. Leshchev, A. Rothenberger, K.C. Neyerlin, D.R. Kauffman, High current density electroreduction of CO₂ into formate with tin oxide nanospheres, *Sci. Rep.* 12 (2022) 8420.
- [45] S.R.D.M. Graciela, T. Baronetti, Osvaldo A. Scelza, Alberto A. Castro, State of metallic phase in Pt-Sn/Al₂O₃ catalysts prepared by different deposition techniques, *Appl. Catal. A* 24 (1986) 109–116.
- [46] Y. Chen, M.W. Kanan, Tin oxide dependence of the CO₂ reduction efficiency on tin electrodes and enhanced activity for tin/tin oxide thin-film catalysts, *J. Am. Chem. Soc.* 134 (2012) 1986–1989.
- [47] X. Cao, B. Wulan, B. Zhang, D. Tan, J. Zhang, Defect evolution of hierarchical SnO₂ aggregates for boosting CO₂ electrocatalytic reduction, *J. Mater. Chem. A* 9 (2021) 14741–14751.
- [48] S. Zhang, M. Sun, K.-Y. Wang, L. Cheng, S. Zhang, C. Wang, Conversion of organically directed selenidostannate into porous SnO₂ exhibiting effective electrochemical reduction of CO₂ to C1 products, *ACS Sustain. Chem. Eng.* 9 (2021) 2358–2366.
- [49] S. Sun, Q. An, M. Watanabe, J. Cheng, H. Ho Kim, T. Akbay, A. Takagaki, T. Ishihara, Highly correlation of CO₂ reduction selectivity and surface electron accumulation: a case study of Au-MoS₂ and Ag-MoS₂ catalyst, *Appl. Catal. B* 271 (2020), 118931.
- [50] F. Lei, W. Liu, Y. Sun, J. Xu, K. Liu, L. Liang, T. Yao, B. Pan, S. Wei, Y. Xie, Metallic Tin quantum sheets confined in graphene toward high-efficiency carbon dioxide electroreduction, *Nat. Commun.* 7 (2016) 12697.
- [51] X. Hou, Y. Cai, D. Zhang, L. Li, X. Zhang, Z. Zhu, L. Peng, Y. Liu, J. Qiao, 3D core-shell porous-structured Cu@Sn hybrid electrodes with unprecedented selective CO₂-into-formate electroreduction achieving 100%, *J. Mater. Chem. A* 7 (2019) 3197–3205.
- [52] F. Wei, T. Wang, X. Jiang, Y. Ai, A. Cui, J. Cui, J. Fu, J. Cheng, L. Lei, Y. Hou, S. Liu, Controllably engineering mesoporous surface and dimensionality of SnO₂ toward high-performance CO₂ electroreduction, *Adv. Funct. Mater.* 30 (2020) 2002092.
- [53] R. He, X. Yuan, P. Shao, T. Duan, W. Zhu, Hybridization of defective Tin disulfide nanosheets and Silver nanowires enables efficient electrochemical reduction of CO₂ into formate and syngas, *Small* 15 (2019), e1904882.
- [54] S. Nakamura, H. Nishikawa, T. Aoki, Y. Ogami, The diffusion overpotential increase and appearance of overlapping arcs on the nyquist plots in the low humidity temperature test conditions of polymer electrolyte fuel cell, *J. Power Sources* 186 (2009) 278–285.
- [55] W. Deng, P. Zhang, B. Seger, J. Gong, Unraveling the rate-limiting step of two-electron transfer electrochemical reduction of carbon dioxide, *Nat. Commun.* 13 (2022) 803.
- [56] Y. Qiu, J. Du, W. Dong, C. Dai, C. Tao, Selective conversion of CO₂ to formate on a size tunable nano-Bi electrocatalyst, *J. CO₂ Util.* 20 (2017) 328–335.
- [57] Q. Zhang, S. Tao, J. Du, A. He, Y. Yang, C. Tao, A cold plasma-activated in situ AgCo surface alloy for enhancing the electroreduction of CO₂ to ethanol, *J. Mater. Chem. A* 8 (2020) 8410–8420.
- [58] S. Zhang, P. Kang, T.J. Meyer, Nanostructured Tin catalysts for selective electrochemical reduction of carbon dioxide to formate, *J. Am. Chem. Soc.* 136 (2014) 1734–1737.
- [59] X. Li, S. Wang, L. Li, Y. Sun, Y. Xie, Progress and perspective for in situ studies of CO₂ reduction, *J. Am. Chem. Soc.* 142 (2020) 9567–9581.
- [60] M. Ocana, C. Serna, J.V. García-Ramos, E. Matijević, A vibrational study of uniform SnO₂ powders of various morphologies, *Solid State Ion.* 63 (1993) 170–177.
- [61] K. Yu, Y. Xiong, Y. Liu, C. Xiong, Microstructural change of nano-SnO₂ grain assemblages with the annealing temperature, *Phys. Rev. B* 55 (1997) 2666.
- [62] C. Meier, S. Lüttjohann, V.G. Kravets, H. Nienhaus, A. Lorke, P. Ifeach, H. Wiggers, C. Schulz, M.K. Kennedy, F.E. Kruijs, Vibrational and defect states in SnOx nanoparticles, *J. Appl. Phys.* 99 (2006), 113108.
- [63] O.M. Berengue, R.A. Simon, A.J. Chiquito, C.J. Dalmascio, E.R. Leite, H. A. Guerreiro, F.E.G. Guimarães, Semiconducting Sn₃O₄ nanobelts: growth and electronic structure, *J. Appl. Phys.* 107 (2010), 033717.
- [64] X.Z. Fengping Wang, Jigang Zhou, Tsun-Kong Sham, Zhifeng Ding*, Observation of single Tin dioxide nanoribbons by confocal Raman microspectroscopy, *J. Phys. Chem. C* 111 (2007) 18839–18843.
- [65] B. Eifert, M. Becker, C.T. Reindl, M. Giar, L. Zheng, A. Polity, Y. He, C. Heiliger, P. J. Klar, Raman studies of the intermediate tin-oxide phase, *Phys. Rev. Mater.* 1 (2017), 014602.
- [66] Y. Yang, S. Ajmal, Y. Feng, K. Li, X. Zheng, L. Zhang, Insight into the formation and transfer process of the first intermediate of CO₂ reduction over Ag-decorated dendritic Cu, *Chemistry* 26 (2020) 4080–4089.

- [67] D. Bohra, I. Ledezma-Yanez, G. Li, W. de Jong, E.A. Pidko, W.A. Smith, Lateral adsorbate interactions inhibit HCOO^- while promoting CO selectivity for CO_2 electrocatalysis on Silver, *Angew. Chem. Int. Ed.* 58 (2019) 1345–1349.
- [68] L. Ma, N. Liu, B. Mei, K. Yang, B. Liu, K. Deng, Y. Zhang, H. Feng, D. Liu, J. Duan, Z. Jiang, H. Yang, Q. Li, In situ-activated indium nanoelectrocatalysts for highly active and selective CO_2 electroreduction around the thermodynamic potential, *ACS Catal.* 12 (2022) 8601–8609.
- [69] Y. Zhao, X. Zu, R. Chen, X. Li, Y. Jiang, Z. Wang, S. Wang, Y. Wu, Y. Sun, Y. Xie, Industrial-Current-Density CO_2 -to- $\text{C}_{(2+)}$ electroreduction by anti-swelling anion-exchange ionomer-modified oxide-derived Cu nanosheets, *J. Am. Chem. Soc.* 144 (2022) 10446–10454.
- [70] B. Zhang, Y. Chang, Y. Wu, Z. Fan, P. Zhai, C. Wang, J. Gao, L. Sun, J. Hou, Regulating $^*\text{OCHO}$ Intermediate as rate-determining step of defective oxynitride nanosheets enabling robust CO_2 electroreduction, *Adv. Energy Mater.* 12 (2022) 2200321.
- [71] Q. Yang, Y. Zhao, L. Meng, Z. Liu, J. Lan, Y. Zhang, H. Duan, Y. Tan, Nanoporous intermetallic SnTe enables efficient electrochemical CO_2 reduction into formate via promoting the fracture of metal-oxygen bonding, *Small* 18 (2022), e2107968.
- [72] J. Duan, T. Liu, Y. Zhao, R. Yang, Y. Zhao, W. Wang, Y. Liu, H. Li, Y. Li, T. Zhai, Active and conductive layer stacked superlattices for highly selective CO_2 electroreduction, *Nat. Commun.* 13 (2022) 2039.
- [73] X. Chen, H. Chen, W. Zhou, Q. Zhang, Z. Yang, Z. Li, F. Yang, D. Wang, J. Ye, L. Liu, Boron dopant induced electron-rich bismuth for electrochemical CO_2 reduction with high solar energy conversion efficiency, *Small* 17 (2021), e2101128.
- [74] W. Shan, R. Liu, H. Zhao, Z. He, Y. Lai, S. Li, G. He, J. Liu, In situ surface-enhanced Raman spectroscopic evidence on the origin of selectivity in CO_2 electrocatalytic reduction, *ACS Nano* 14 (2020) 11363–11372.
- [75] D. Chen, L.H. Zhang, J. Du, H. Wang, J. Guo, J. Zhan, F. Li, F. Yu, A tandem strategy for enhancing electrochemical CO_2 reduction activity of single-atom $\text{Cu-S}_1\text{N}_3$ catalysts via integration with Cu nanoclusters, *Angew. Chem. Int. Ed.* 60 (2021) 24022–24027.
- [76] Q. Lu, J. Rosen, Y. Zhou, G.S. Hutchings, Y.C. Kimmel, J.G. Chen, F. Jiao, A selective and efficient electrocatalyst for carbon dioxide reduction, *Nat. Commun.* 5 (2014) 3242.
- [77] J.T. Feaster, C. Shi, E.R. Cave, T. Hatsukade, D.N. Abram, K.P. Kuhl, C. Hahn, J. K. Nørskov, T.F. Jaramillo, Understanding selectivity for the electrochemical reduction of carbon dioxide to formic acid and carbon monoxide on metal electrodes, *ACS Catal.* 7 (2017) 4822–4827.
- [78] S. Zhu, B. Jiang, W.B. Cai, M. Shao, Direct observation on reaction intermediates and the role of bicarbonate anions in CO_2 electrochemical reduction reaction on Cu surfaces, *J. Am. Chem. Soc.* 139 (2017) 15664–15667.
- [79] Y. Hori, H. Wakebe, T. Tsukamoto, O. Koga, Electrocatalytic process of selectivity in electrochemical reduction of CO_2 at metal electrodes in aqueous media, *Electrochim. Acta* 39 (1994) 1833–1839.